Effects of causally driven cusp O^+ outflow on the storm time magnetosphere-ionosphere system using a multifluid global simulation

O. J. Brambles,[1] W. Lotko,[1] P. A. Damiano,[1] B. Zhang,[1] M. Wiltberger,[2] and J. Lyon[3]

Received 16 March 2010; revised 23 April 2010; accepted 1 June 2010; published 25 September 2010.

[1] It is widely accepted that the ionosphere is an important source of ions in the magnetosphere and until recently this population has largely been neglected from many global simulations. In this study, a causally regulated cusp O^+ outflow is added to the multifluid version of the Lyon-Fedder-Mobarry (LFM) global simulation. The cusp outflow algorithm uses empirical relationships to regulate the outflow flux with further conditioning to isolate the outflow spatially to a dynamic cusp. The impact cusp O^+ outflow has on the magnetosphere-ionosphere (MI) system is investigated for a moderate storm on 31 August 2005. It is found the MI system response depends upon the specification of the outflow velocity and temperature. More energetic outflow tends to flow downtail whilst colder, slower outflow fills the inner magnetosphere. High O^+ densities in the inner magnetosphere can increase the strength of the ring current, reducing Dst and inflating the magnetosphere. This effect is mostly found for the less energetic outflow specification. O^+ outflow is found to reduce the access of solar wind ions to the inner magnetosphere, which, through the MI coupling in LFM reduces the precipitating electron power, conductance and field-aligned currents. The effect outflow has on the cross polar cap potential (CPCP) depends upon two competing factors. The reduction in Region I currents when outflow is present appears to increase the CPCP whilst the inflation of the magnetosphere due to an enhanced ring current decreases the CPCP.

Citation: Brambles, O. J., W. Lotko, P. A. Damiano, B. Zhang, M. Wiltberger, and J. Lyon (2010), Effects of causally driven cusp O^+ outflow on the storm time magnetosphere-ionosphere system using a multifluid global simulation, *J. Geophys. Res.*, *115*, A00J04, doi:10.1029/2010JA015469.

1. Introduction

[2] It is widely accepted that there are two main sources of plasma in the magnetosphere, the solar wind and the ionosphere. *Shelley et al.* [1972] were the first to reveal the ionosphere as an important source of magnetospheric plasma by discovering a population of O^+ ions in the magnetosphere using data from polar-orbiting satellite 1971-089A.

[3] The main mechanism that can accelerate O^+ ions from the ionosphere into the magnetosphere is transverse ion acceleration by wave-particle interactions [*Norqvist et al.*, 1998], accompanied by mirror force lifting which is directly proportional to the perpendicular ion energy. The first direct observation of energetic (keV), outward flowing ions in the auroral regions (64° to 80° latitude) was provided by *Shelley et al.* [1976]. Transverse ion heating and acceleration in the auroral zone was observed by *Whalen et al.* [1978] and *Klumpar* [1979]. The heated ions range in energy from tens of eV up to several keV [*Hultqvist et al.*, 1991; *Yau and André*, 1997]. Further studies have shown transversely accelerated ions are found throughout the auroral regions and, to a lesser extent, the polar cap [*Gorney et al.*, 1981; *Yau et al.*, 1985] with the dayside cusp and cleft region providing the largest fluxes of O^+ ions [*Lockwood et al.*, 1985a, 1985b; *Thelin et al.*, 1990].

[4] It has been suggested that resonant energization by broadband low-frequency waves is the most important mechanism for the energization of O^+ ions [*Norqvist et al.*, 1998]. This heating acts to increase the perpendicular energy of the ions. The increased perpendicular energy of the ions is progressively converted into parallel energy by the mirror force. The ion is accelerated to velocities high enough to escape gravity and outflow into the magnetosphere [*Bouhram et al.*, 2004]. Heavy ions, such as O^+ are more easily accelerated by this process owing to their relatively large gyroradii. The first adiabatic invariant of the heavier ions is more easily broken by intense, small scale electric fields that develop through turbulent cascades, phase mixing and micro-instabilities.

[5] Global magnetohydrodynamic (MHD) simulation models are becoming a major tool to aid in the understanding of

[1]Thayer School of Engineering, Dartmouth College, Hanover, New Hampshire, USA.
[2]High Altitude Observatory, National Center for Atmospheric Research, Boulder, Colorado, USA.
[3]Department of Physics and Astronomy, Dartmouth College, Hanover, New Hampshire, USA.

0148-0227/10/2010JA015469

the impact of ionospheric outflows on the magnetosphere-ionosphere (MI) system. Investigations into the effects of outflowing ions in global magnetosphere simulations began with *Winglee* [1998]. In Winglee's simulations the O^+ ions are gravitationally bound at the inner boundary and require either pressure gradients or centrifugal acceleration for them to outflow into the magnetospheric domain. *Winglee et al.* [2002] found that when outflow is included in the global simulation, the cross polar cap potential (CPCP) is significantly reduced compared to simulations without outflow, suggesting the importance of ion outflow on the MI coupled system.

[6] *Gagne* [2005] developed an outflow model that used the *Strangeway et al.* [2005] empirical relationships between ion outflow and D.C. Poynting flux and electron precipitation number flux to add outflow to the single-fluid version of the Lyon-Fedder-Mobarry (LFM) global simulation. Unlike the studies by Winglee, the simulation allowed for feedback of the outflow on the ionosphere through modification of the electron precipitation characteristics and hence, the conductance. It was found that this feedback was responsible for an increase in the CPCP when outflow was added, contrary to the studies by *Winglee et al.* [2002].

[7] *Glocer et al.* [2009a] added a polar wind model (named PWOM) to the BATS-R-US (Block Adaptive Tree Solar wind Roe type Upwind Scheme) global simulation. PWOM is coupled to ionospheric electrodynamics and the magnetosphere and covers the gap region that exists between the ionospheric and magnetospheric domains. PWOM takes its input from the Michigan Global-Ionosphere-Thermosphere model [*Ridley et al.*, 2006] and calculates the outflow fluxes at the top of the flux tube which are used at the inner boundary of the simulation domain to specify outflow. Both multispecies [*Glocer et al.*, 2009a] and multifluid [*Glocer et al.*, 2009b] versions of BATS-R-US have been investigated using this technique. *Glocer et al.* [2009a] found that this specification of outflow caused a decrease in CPCP and when BATS-R-US was also coupled to the Rice Convection Model (RCM), the simulation Dst was enhanced.

[8] This study aims to further the work by *Gagne* [2005] by using satellite data to implement a causally driven, cusp O^+ outflow algorithm in the Multifluid Lyon-Fedder-Mobarry (MFLFM) global simulation. The outflow is conditioned to be released only in a dynamically regulated cusp region. By isolating the outflow to the cusp, the effects of cusp O^+ outflow on the coupled MI system during storm time conditions can be examined and distinguished from effects attributed to other types of outflow, e.g. polar wind and auroral outflows. The findings from this study are then compared to the results from *Glocer et al.* [2009a], *Winglee et al.* [2002, 2005], and *Gagne* [2005].

[9] The paper introduces the equations of the MFLFM global simulation (Section 2), and describes the physical motivation for the techniques used to generate the dynamically regulated cusp outflow (Section 3) and an investigation into the effects of the O^+ outflow on the MI system for the 31 August 2005 storm (Section 4).

2. Multifluid Lyon-Fedder-Mobarry (MFLFM) Model

[10] The model used is a multifluid adaptation of the Lyon-Fedder-Mobarry (LFM) global simulation code [*Lyon et al.*, 2004; J. Lyon and V. Merkin, Multifluid equations for MHD, submitted to *Journal of Geophysical Research*, 2010]. It uses the equations

$$\frac{\partial \rho_\alpha}{\partial t} = -\nabla \cdot \rho_\alpha \mathbf{u}_\alpha, \tag{1}$$

$$\frac{\partial \mathbf{p}_\alpha}{\partial t} = -\nabla \cdot (\mathbf{p}_\alpha \mathbf{u}_\alpha + \mathbf{I} P_\alpha) + \mathbf{F}^d_\alpha + n_\alpha q_\alpha \mathbf{E}_\parallel, \tag{2}$$

$$\frac{\partial \epsilon_\alpha}{\partial t} = \nabla \cdot \mathbf{u}_\alpha (\epsilon_\alpha + P_\alpha) + \mathbf{u}_\alpha \cdot (\mathbf{F}^d_\alpha + n_\alpha q_\alpha \mathbf{E}_\parallel), \tag{3}$$

$$\frac{\partial \mathbf{B}}{\partial t} = -\nabla \times (\mathbf{u} \times \mathbf{B}), \tag{4}$$

where ρ, $\mathbf{p}$, $\mathbf{u}$, P and ϵ are the mass density, momentum, velocity, pressure and plasma energy respectively with subscripts α and β representing the individual ion species. $\mathbf{B}$ is the magnetic field, the ambipolar electric field is given by $\mathbf{E}_\parallel = -\hat{b}\hat{b} \cdot \nabla P_e / ne$ where P_e is the electron pressure and $\epsilon_\alpha = \frac{1}{2} P_\alpha \mathbf{u}^2_\alpha + \frac{P}{\gamma - 1}$. $\mathbf{F}^d_\alpha$ is the Lorentz force that includes a first order ion drift in the expansion parameter $1/\omega_{c\alpha}\tau$ where ω_c is the gyrofrequency and τ is an MHD time scale. $\mathbf{F}^d_\alpha$ is given by

$$\mathbf{F}^d_\alpha = \hat{b} \times \left[\mathbf{p}_\alpha \cdot \nabla \mathbf{u}_\alpha + \nabla P_\alpha + \frac{\rho_\alpha (\mathbf{u}_M - \mathbf{u}_\alpha) \cdot \hat{b}}{B} \frac{\partial B}{\partial t} \right] - \frac{\rho_\alpha}{\rho} \left(\sum_\beta (\mathbf{p}_\beta \cdot \nabla \mathbf{u}_\beta + \nabla P_\beta) + \nabla P_e - \mathbf{j} \times \mathbf{B} \right)] \times \hat{b},$$

where $\hat{b} = \mathbf{B}/B$, $\mathbf{u}_M$ is the total bulk velocity and $\mathbf{j}$ is the current density. In the simulation, the two ion species have the same $\mathbf{E} \times \mathbf{B}$ drifts perpendicular to the ambient magnetic field with individual diamagnetic and inertial drifts. The flow parallel to $\mathbf{B}$ of the two species is coupled via the parallel electric field. Within the model, the electron pressure is specified as a fraction of the total ion pressure and locally partitioned between the ion species based on the relative ion species fractions. In this present study however, we assume that the electrons are a cold neutralizing fluid with zero temperature and pressure which facilitates understanding the system in a simpler limit. Further discussion is given by *Lyon and Merkin* [2010]. The implications of the zero electron pressure on the simulation dynamics are discussed in section 4.1.

[11] The computational grid for the LFM domain spans from 25 R_E to −300 R_E along the SM x-axis (sun-earth line) and ±100 R_E along the y-axis (dusk-dawn) and z-axis (north-south). The grid is non-orthogonal with finer grid resolution in areas of interest such as the bow shock and inner magnetosphere. The grid resolution ranges from 0.25–0.50 R_E in the inner magnetosphere and bowshock, increasing to 1–2 R_E in the region of nightside reconnection and approximately 15–20 R_E at distances greater than 100 R_E.

[12] A finite volume method is used to solve the MHD equations describing mass, momentum and energy conservation. The total variation diminishing finite volume algorithm used in the model operates on a *Yee* [1966] grid that

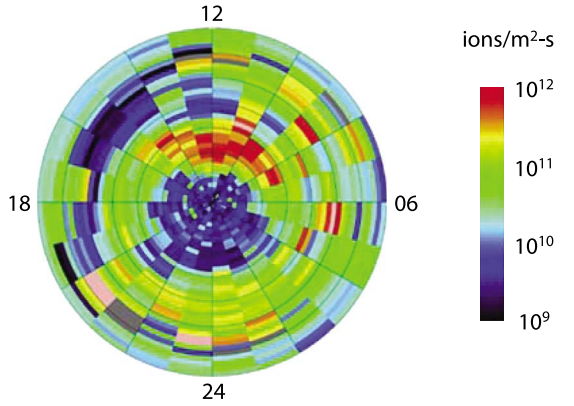

Figure 1. Normalized O^+ ion flow densities from *Lennartsson et al.* [2004].

allows for easy implementation of $\nabla \cdot \mathbf{B} = 0$ condition. The inner boundary of LFM is a sphere with a radius of 2 R_E. Below this altitude the plasma can no longer be described as collisionless and the ideal MHD equations are no longer valid. An electric field and convection velocity are imposed on the plasma fluid at the low-altitude grid cell and are controlled via the coupling of the magnetosphere to an ionospheric model. The ionosphere model solves for the ionospheric potential using a thin spherical shell approximation given by

$$\nabla \cdot \overline{\Sigma} \cdot \Psi = j_{\parallel} \sin \delta, \tag{5}$$

where $\overline{\Sigma}$ is the conductance tensor, Ψ is the electrostatic potential, $j_{\parallel}$ is the field-aligned current mapped to the ionosphere from the low-altitude simulation boundary and δ is the magnetic dip angle. The conductances are calculated using empirical models for both the EUV-induced and precipitation-induced ionization. The EUV-induced conductance is parameterized by the $F_{10.7}$ flux and the solar zenith angle. The precipitation-induced conductances use the *Robinson et al.* [1987] formulas for the Hall and Pedersen conductances with precipitating energy and flux derived from the MHD state variables at the low-altitude simulation boundary [*Fedder et al.*, 1995; *Wiltberger et al.*, 2009]. The electric potential obtained from (5) is then mapped out to the inner boundary where the electric field, **E** and corresponding **E** × **B** convection velocity are calculated and imposed.

3. Outflow Model

3.1. Observational Motivation

[13] The cusp O^+ outflow model used here is motivated primarily by observational results reported by *Strangeway et al.* [2005], *Bouhram et al.* [2004], and *Lennartsson et al.* [2004]. These studies characterize and quantify O^+ outflow properties using in situ satellite data. Including outflow in an MHD simulation requires specification and regulation of the addition of mass, momentum and internal energy of the outflow in each computational cell at the low-altitude boundary.

[14] *Lennartsson et al.* [2004] investigated how the solar wind controls H^+ and O^+ outflow fluxes in the 15 eV to 33 keV range at altitudes near 1 R_E altitude corresponding to the low-altitude boundary of the MFLFM simulation. Transversely accelerated ions are observed in this energy range. *Lennartsson et al.* [2004] found that outflow fluences are up to twice as high for periods of southward IMF compared to northward IMF. It is well-known that the magnetosphere is more highly energized during periods of southward IMF, e.g., the CPCP and Joule dissipation in the ionosphere are greater, and the results of *Lennartsson et al.* [2004] indicate theat O^+ fluxes are also enhanced during such intervals. Figure 1 shows the statistical locations of outflow source regions reported by *Lennartsson et al.* [2004], all mapped to the same reference altitude of 300-km. Peaks in the outflow flux are evident in the cusp and to a lesser extent in the auroral regions. This study suggests that the cusp is statistically the main source of O^+ outflows, at least at O^+ energies exceeding the ion detector's energy threshold of 15 eV.

[15] FAST satellite measurements have been used to investigate the factors that control O^+ outflows observed at 4000-km altitude in the region of the cusp during the 24–25 September 1998 storm [*Strangeway et al.*, 2005]. The ion outflow is correlated with both D.C. Poynting flux and the number flux of soft (<100 eV) electron precipitation, as shown in Figure 2. *Strangeway et al.* [2005] suggest two main pathways for the acceleration of O^+ ions. One pathway is through electromagnetic energy deposition into the lower ionosphere, fed by Poynting flux, whilst the other involves particle energy deposition (predominantly soft electron precipitation) in the topside ionosphere. The electric fields associated with Poynting fluxes result in ion frictional heating due to collisions with neutral particles. This process increases the ionospheric scale height and F-region peak altitude. Electron precipitation heats ionospheric electrons, increasing the topside scale height through ambipolar electric fields. Soft electrons are required as high energy electrons penetrate too deeply into the ionosphere. Whilst both processes result in ionospheric upwelling, transverse wave heating is required to generate ion conics that can then escape gravity. It has been suggested that field-aligned currents associated with Poynting flux and/or precipitating electrons can generate ELF waves through current driven instabilities to further energize the ions [*Yau and André*, 1997]. Direct energization via the intense small scale electric fields of Alfvén waves is also a possible mechanism [*Chaston et al.*, 2007].

[16] Building on the analysis by *Strangeway et al.* [2005], *Zheng et al.* [2005] used Polar satellite data to investigate the drivers of O^+ outflow. Their data sample included local times other than the cusp and was taken over an entire year, rather than for a single storm interval as in the *Strangeway et al.* [2005] study. The results confirm correlations reported in the study by *Strangeway et al.* [2005]. However, it was found that for a given energy input the average ion fluxes were weaker (Figure 2). This result is not surprising given that *Peterson et al.* [2002] found a variability in the magnitude in the outflow fluxes at low and moderate activity levels (A_E < 500 nT) of about four orders of magnitude. Whilst these results suggest that D.C. Poynting flux and/or electron precipitation alone are not sufficient to predict outflow, they are, to date, the most useful empirical relationships for specifying and regulating outflow in global MHD

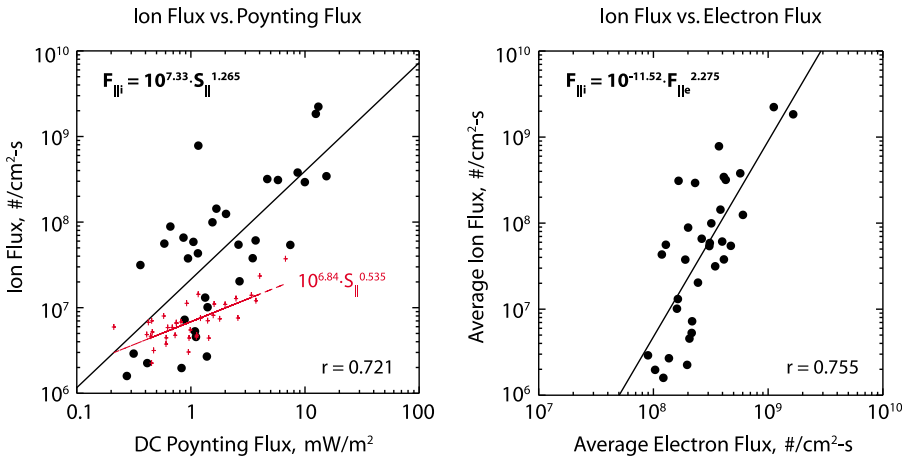

Figure 2. Empirical relations between (left) O^+ outflow flux and D.C. Poynting flux and (right) precipitating electron number flux derived from FAST satellite data obtained near 4000-km altitude (black dots [*Strangeway et al.*, 2005]) and Polar satellite data obtained near 1 R_E altitudes (red dots [*Zheng et al.*, 2005]).

simulations. The outflow model given in Section 3.2 uses the *Strangeway et al.* [2005] empirical relationships to drive outflow, concentrating on cusp outflow during storm time solar wind conditions.

[17] *Bouhram et al.* [2004] studied the altitude dependence of transversely accelerated O^+ outflow in the cusp region. A mean outflow velocity of 30–50 km/s and temperatures of 100 eV were found at 2 R_E (geocentric), and these values progressively increased with altitude to an average velocity of 70–150 km/s and temperature of 400–800 eV at 4.3 R_E. The flux and density of the outflow were found to vary greatly with conditions with smaller variations in the temperature and field-aligned velocity. Since the velocity and temperature of observed O^+ outflows exhibit less variability relative to the density, for simplicity and lacking a good physical model, these two parameters will be taken as constants, independent of time and space in the outflow specification. The outflow flux is the constrained by the *Strangeway et al.* [2005] empirical relation given below in (6), and, since the flux is a product of density and field-aligned velocity, which is constant, the density of the outflow is directly proportional to the flux.

3.2. Outflow Algorithm

[18] The outflow algorithm simulates causally driven O^+ outflow from the cusp and is a continuation of the work of *Gagne* [2005]. The model uses downward, field-aligned D.C. Poynting flux to calculate the O^+ outflow flux, given by the empirical formula [*Strangeway et al.*, 2005]

$$F_{\mathrm{O}} = 2.14 \times 10^7 S_{\parallel}^{1.265}, \tag{6}$$

where F_O is the O^+ outflow flux in units of cm^2-s and $S_\parallel$ is the field-aligned DC Poynting flux in units of mW/m^2 calculated as

$$S_{\parallel} = \frac{\mathbf{E} \times \delta\mathbf{B}}{\mu_o} \cdot \mathbf{b}, \tag{7}$$

where $\mathbf{b} = \mathbf{B}/|B|$, $\mathbf{E}$ is the electric field and $\delta\mathbf{B}$ is the difference between the simulation magnetic field and dipole magnetic field. The Poynting flux is calculated at 3 R_E (geocentric) in the magnetosphere domain and mapped down to 4000-km altitude where (6) is valid. 3 R_E is chosen as a compromise between maximizing the Poynting flux that increases with altitude (numerical effects lead to a reduction in $S_\parallel/B_{dip}$ close to the inner boundary) and the practical consideration of allowing the Poynting flux to map to as low a latitude as possible.

[19] The D.C. Poynting flux is actually relatively indiscriminate in regulating outflow in the simulation, e.g., D.C. Poynting fluxes feed currents closing over the polar cap and at low latitudes where Region I and Region II current systems close with each other. These regions of D.C. Poynting flux must be masked in the simulation in order to limit the outflow to the cusp. In the model, (6) is modified through the use of three additional regulating functions:

$$F_{\mathrm{O}'} = 2.14 \times 10^7 S_{\parallel}^{1.265} M_x M_{v_x} M_{F_{en}}, \tag{8}$$

where M_x and M_{vx} are spatial and convection velocity masks and $M_{F_{en}}$ is a regulator based on the electron number flux (F_{en}), derived from the MFLFM precipitating precipitation model. These masks restrict the outflow to the cusp, the region of interest for this study and are described in more detail in Appendix A.

[20] Equation (8) represents the O^+ outflow flux at 4000-km altitude. This flux is mapped to the inner boundary of the MFLFM computational domain of 2 R_E (geocentric) assuming F_O/B is constant. To be consistent with *Bouhram et al.* [2004] for transversely accelerated outflow the parallel velocity of the outflow is set to 50 km/s with a temperature of 100 eV. The greatest variability in the observed outflow flux reported by *Bouhram et al.* [2004] at 2.3 R_E geocentric is due to variations in the density. The outflow velocity and temperature, according to *Bouhram et al.* [2004], exhibit less variability and so for this simulation they are treated as constant in space and time. The density, n is calculated from $n = F_O/v_\parallel$ where F_O is the field-aligned outflow flux and $v_\parallel$ is the constant outflow velocity. The pre-specified parallel velocity is added to the first active (i = 1) cells convection

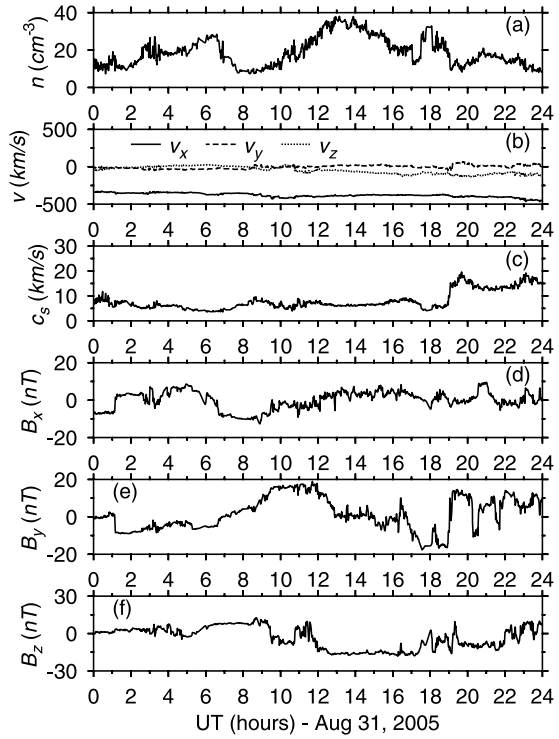

Figure 3. Solar wind parameters for 31 August 2005 storm.

velocity as determined by the ionospheric potential solver. The density and the pre-specified temperature are then imposed at the first active cell.

[21] For this simulation, the O^+ fluid is neglected from the calculation of the electron characteristic energy and flux. Only precipitating electrons that have energies greater than approximately 1 keV should contribute to the regulation of outflow. This choice maintains the causality of the outflow algorithm as cold electron upwelling with O^+ ions, if backscattered do not affect the height integrated conductance. Their energy is deposited at altitudes where the collision frequency is too small for perpendicular currents to be sustained [*Robinson et al.*, 1987]. This choice, however, also neglects the effect of the recirculated O^+ fluid on the electron characteristic energy and flux. The implications of this assumption on the simulation results are discussed in section 4.3.

4. Storm Simulation

[22] The outflow algorithm has been used to investigate the effects and characteristics of cusp outflow for the 31 August 2005 storm. The storm is classed as "moderate" with a minimum Dst of −140 nT and negative B_z of −18 nT during a 5-hour encounter with an interplanetary magnetic cloud. The summary of the upstream conditions at x_{SM} = 30 R_E in the solar wind during the storm can be seen in Figure 3. The 1-minute data samples in the figure were obtained from OMNI data set at http://cdaweb.gsfc.nasa.gov/istp_public and using v_x from the solar wind data have been ballistically propagated to the upstream boundary of the MFLFM simulation at 30 R_E. Assuming no variation in y_{SM} or z_{SM} of the upstream variables, the solar wind density, velocity and sound speed and the IMF B_y and B_z are used as boundary conditions to drive the simulation. As is typical in the LFM global simulation, driven by actual event data, IMF B_x is artificially set to zero to ensure $\nabla \cdot \mathbf{B} = 0$. Two outflow cases were simulated in addition to a control baseline simulation with no outflow. Both cases had the same dynamically regulated outflow flux that is calculated from equation (8) but used different specifications of the outflow velocity and temperature at the inner boundary. Outflow case A used outflow specifications of a constant velocity of 50 km/s and a temperature of 100 eV, to be approximately consistent with the statistical results reported by *Bouhram et al.* [2004] for transversely accelerated O^+ outflows observed at 2.3 R_E geocentric. Case B had a different constant parallel velocity of 3 km/s and temperature of 1 eV. This outflow specification represents a colder, slower, and denser population of outflowing ions. Whilst this colder and slower outflow specification is not consistent with the observations reported by *Bouhram et al.* [2004] for transversely accelerated O^+ ions, it not only serves as an interesting experiment but represents outflow characteristics more consistent with the studies by *Winglee et al.* [2002] and *Glocer et al.* [2009a]. For example, at the inner boundary in the study by *Winglee* [1998], the O^+ ions are specified with zero velocity and have temperatures ranging from 10 eV at the equator to 0.1 eV at the poles. *Glocer et al.* [2009a] model polar wind outflows that typically have temperatures of <1.4 eV and velocities of <3 km/s at 5,000-km altitude and are representative of the Polar TIDES data reported by *Su et al.* [1998]. The simulation parameters are summarized in Table 1.

4.1. Outflow Properties

[23] Figure 4 shows the O^+ fluence in the northern and southern ionospheres (Figure 4a) for case A, the solar wind dynamic pressure at the upstream boundary of the LFM global simulation (Figure 4b) and the IMF B_z at the LFM model's upstream boundary superimposed on Dst (Figure 4c). The simulated outflow is controlled by both B_z and solar wind dynamic pressure, which influence the Poynting flux flowing into the ionosphere from the solar-wind (SW) dynamo (B_z) and the area of cusp outflow region (P_{dyn}) [see *Damiano et al.*, 2010; *Newell et al.*, 2006]. The fluence in the northern hemisphere peaks at 1.6×10^{26}/s and the outflow flux when mapped to the ionosphere at 100-km peaks at 1.7×10^{13} ions/m^2/s.

[24] Examples of outflow patterns during the storm can be seen in Figure 5 for case A. The figure shows outflow flux, with convection lines (white) and the location of last closed field line (black) superimposed. The outflow is located in the convection throat, at latitudes and local times consistent

Table 1. Outflow Specification at Inner Boundary for Simulations in the Study

Simulation	$v_{\parallel}$ (km/s)	T_i (eV)	$F_{\parallel}$	n_{O+}
Baseline	N/A	N/A	N/A	N/A
Case A	50	100	equation (8)	$F_{\parallel}/v_{\parallel}$
Case B	3	1	equation (8)	$F_{\parallel}/v_{\parallel}$

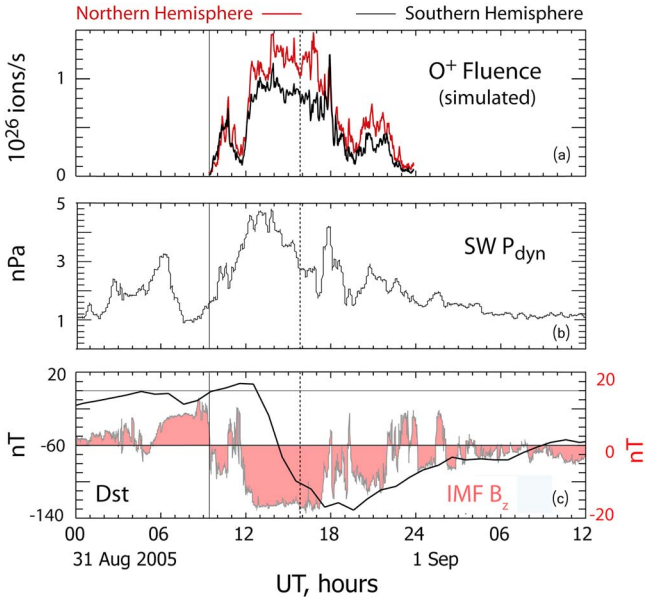

Figure 4. August 31, 2005 storm characteristics. (a) O^+ fluence in the northern and southern ionospheres, (b) the solar wind dynamic pressure at LFM's upstream boundary, and (c) the IMF B_z at the LFM global model's upstream boundary superimposed on Dst.

with the observations of *Lennartsson et al.* [2004]. The position of the outflow also correlates well to the so-called polar cusp heating wall [*Knudsen et al.*, 1994] wherein the transverse heating that initiates O^+ outflow begins 1–2° poleward of the open-closed field boundary. The summer hemisphere has higher outflow fluence than the winter hemisphere, which is also consistent with the statistical results of *Lennartsson et al.* [2004]. The difference occurs in the simulation because the D.C. Poynting flux, which controls the outflow, is larger in the summer hemisphere than in the winter ionosphere. Observations of ionospheric joule dissipation exhibit similar seasonal dependence [*Chun et al.*, 2002]. To explain this effect, we can ignore the minor power consumed by particle acceleration through field-aligned potential drops ($j_{\|}\Delta\Phi_{\|}$) in the gap region of the MFLFM model and consider the field-aligned Poynting flux at the low-altitude simulation boundary equal to the ionospheric joule dissipation:

$$S_{\|i} = \Sigma_P E_i^2. \tag{9}$$

$S_{\|i}$ is the Poynting flux mapped to the ionosphere ($S_{\|}/B$ is constant), Σ_P is Pedersen conductivity and E_i is the magnitude of the perpendicular electric field at the ionosphere. The summer ionosphere has a larger Pedersen conductance due to the increased solar EUV-induced ionization that causes the increased D.C. Poynting flux. In a simple circuit analogy the summer and winter ionospheres can be treated like two resistors connected in parallel to a common voltage or current generator representing the SW dynamo. In such a circuit, more power flows into the resistor with the higher conductance.

[25] In comparing the different impacts on the magnetosphere in simulations A and B it is informative first to examine differences in the spatial propagation of the outflow between the two cases. Figure 6 shows a comparison of the outflow fluxes at 6 R_E geocentric. For case B the outflow plume has convected more poleward than case A at 6 R_E geocentric due to its slower parallel velocity. The cusp outflow is transported across the polar cap and into the lobes where it either enters the plasma sheet and is convected into the inner magnetosphere, consistent with observations from Cluster data by *Kistler et al.* [2010] or the outflow flows downtail. The higher initial $v_{\|}$ of the outflow in case A causes it to mainly flow downtail whilst the smaller $v_{\|}$ of case B allows more of the outflow to fill the inner magnetosphere (Figure 7). These results are consistent with particle simulations showing that O^+ ions with a temperature of 100 eV and $v_{\|}$ of 50 km/s from the cusp would flow mainly downtail whilst ions with a temperature of 1 eV and $v_{\|}$ of 3 km/s would primarily contribute to the ring current [*Ebihara et al.*, 2006].

[26] The O^+ ions populate four distinct regions: the low-altitude cusp, the lobes, the plasmasheet and the inner magnetosphere. At low-altitude, outflowing O^+ ions counterstream through downflowing H^+ ions. With zero electron pressure the relative parallel motion of the fluids is uncoupled.

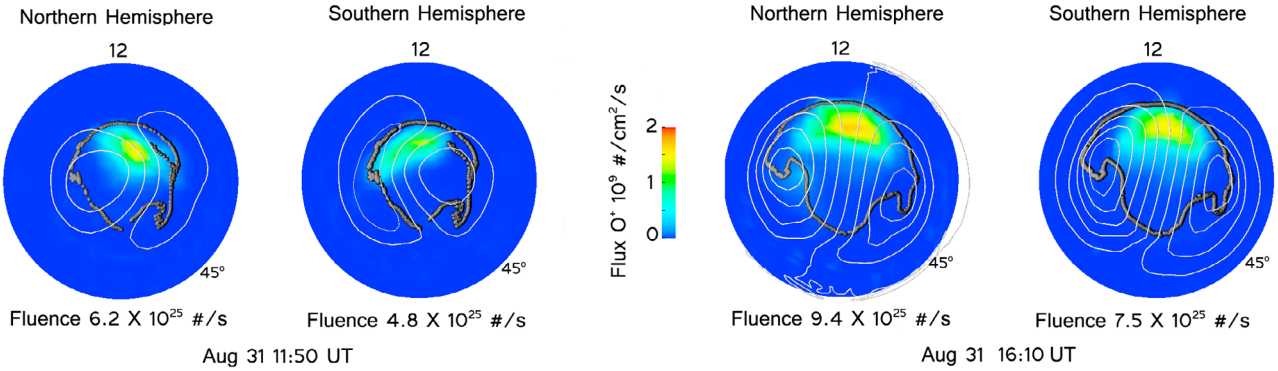

Figure 5. Example O^+ outflow fluxes for case A for the 31 August 2005 storm. (Left) Outflow pattern at 11:50 UT. (Right) Outflow pattern at 16:10 UT during the long magnetic cloud encounter with IMF $B_z < 0$.

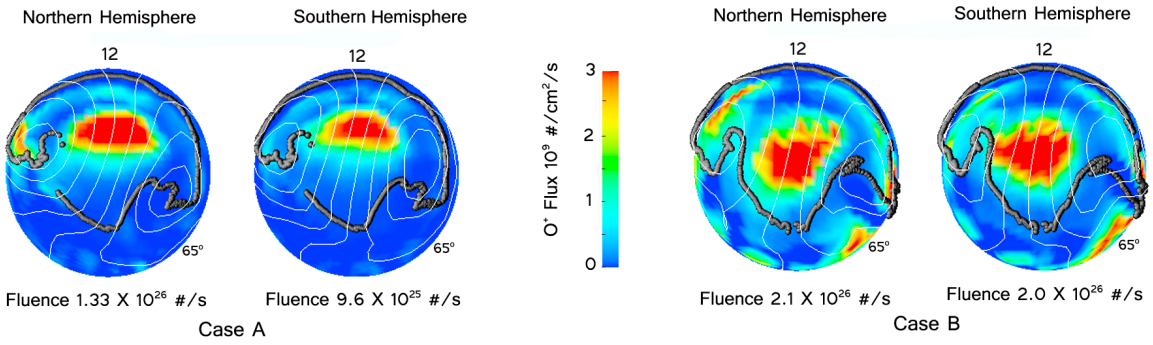

Figure 6. Outflow fluxes for (left) case A and (right) case B at 6 R_E geocentric at 1500 UT.

If electron pressure were included the resulting ambipolar electric field would tend to retard the parallel acceleration of the O^+ outflow. The region of counterstreaming extends over approximately 1 R_E, and therefore, this effect on the simulation is expected to be minimal. In the lobes and the plasmasheet the lack of electron pressure should not affect the plasma dynamics. The low H^+ density in the lobes implies that the ambipolar electric field in this region will also be small. The ion motion in the plasmasheet and inner magnetosphere are governed primarily by perpendicular forces and therefore electron pressure does not play a major role in the dynamics of this region. We anticipate that the inclusion of electron pressure would be a minor correction to the results presented in this paper and the effect will be addressed in a future study.

4.2. Plasmasheet and Inner Magnetosphere

[27] The outflow in case A flows mainly downtail with a small portion flowing into the region of nightside reconnection. The fraction of the outflowing fluid that interacts with the reconnection process is evidently sufficient to cause nightside reconnection to migrate earthward. In a simple model the rate of reconnection is proportional to the Alfvén speed in the reconnection inflow region. The Alfvén speed is given by $V_A = B/\sqrt{\mu_0 \rho}$ where B is the magnetic field, μ_0 is the permeability of free space and ρ is the mass density. The addition of O^+ ions to the reconnection region increases the local mass density and, hence, reduces the Alfvén speed and the reconnection inflow velocity. During the main phase of the storm the IMF conditions are reasonably steady and therefore to the extent that the dayside and nightside reconnection rates are in balance, in order to maintain the same nightside reconnection rate when outflowing plasma enters the inflow region, the reconnection point must move earthward to a location of higher magnetic field to offset the increase in mass and density associated with the outflow. An alternative explanation is that the O^+ ions that land in the equatorial plane builds up a pressure tailward of the reconnection region. The resulting pressure gradient then pushes the reconnecting field lines earthwards. The change in reconnection location when outflow is added is shown in Figure 8. The nightside reconnection moves from 20 R_E in the baseline simulation to 15 R_E with case A outflow.

[28] The change in location of nightside reconnection reduces the access of the solar wind proton fluid to the inner magnetosphere. During intervals of southward IMF, the solar wind populates the inner magnetosphere via cusp/mantle entry, followed by convective transport through the lobes and plasmasheet [*Pilipp and Morfill*, 1978; *Siscoe et al.*, 2001], taken here to be the hot, dense plasma region earthward of the nightside reconnection region. For this storm the plasmasheet is initially filled with plasma of solar wind origin, mainly following this path. However, the access to the plasmasheet from cusp/mantle streamlines also depends on the location of the nightside reconnection, which, as shown in Figure 8, changes when ionospheric cusp outflow is

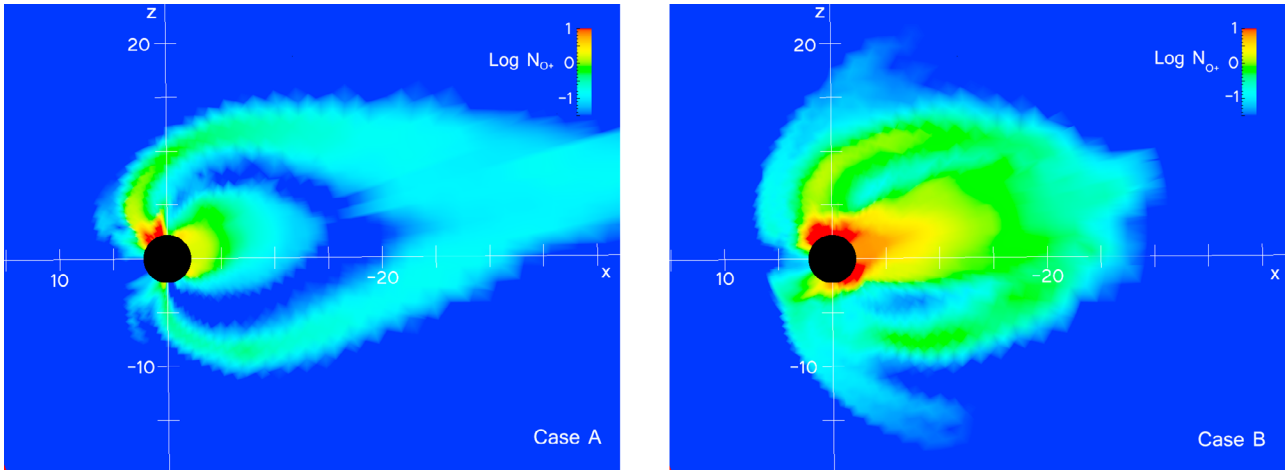

Figure 7. Logarithm O^+ number density for (left) case A and (right) case B in x-z GSM plane at 1500 UT.

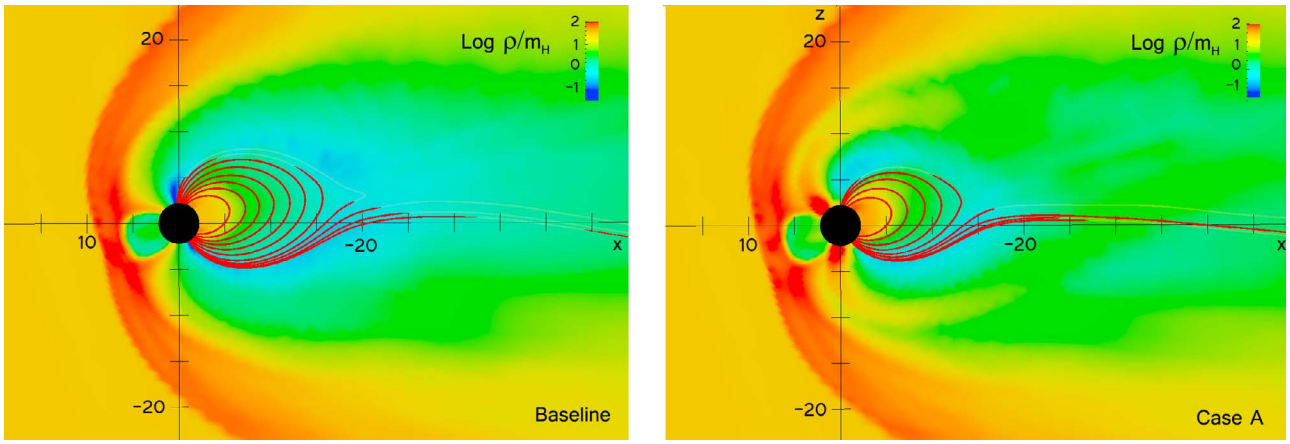

Figure 8. Logarithm density of the total fluid, normalized to proton mass for (left) baseline and (right) case A in the x-z GSM plane at 1500 UT. Select magnetic field lines are superimposed.

present. If the ratio of average $v_{||}/v_{\perp}$ along cusp/mantle/lobe streamlines depends only weakly on the location of nightside reconnection, then when the nightside reconnection region moves closer to earth, the access of solar wind plasma to the plasmasheet is correspondingly diminished. This reduction decreases the contribution of H^+ of solar wind origin to the plasma density and pressure of the inner magnetosphere. For case A, $v_{||}/v_{\perp}$ is, in fact, approximately the same as the baseline case, and the accumulation of H^+ plasma density and pressure for case A in the inner magnetosphere is less than the baseline by about 50% following the earthward migration of the reconnection line.

[29] The O^+ fluid convected into the inner magnetosphere offsets the loss of plasma pressure due to the reduced H^+ pressure. In the inner magnetosphere, the O^+ density is approximately 3/cc, compared to 10/cc for the H^+ fluid. The change in pressure gradients in the inner magnetosphere alters the MHD diamagnetic ring current. Figure 9 shows the actual Dst, a measure of the strength of the ring current compared to the simulated, pseudo Dst for the storm interval for both baseline, case A and case B simulations. The pseudo Dst for the simulation is calculated from the Biot-Savart law integral, evaluated at the centre of the Earth, including contributions from all currents in the simulation domain. The magnetic field component in the z-direction from the Biot-Savart law calculation is used as the pseudo Dst [A. Glocer, private communication, 2009], including a 45 nT offset so that it matches the actual Dst during quiet solar wind conditions. This offset is analagous to the magnetic field depression at geocentric distances of 2.3 to 3.6 R_E when the Dst is 0 [*Suguira*, 1973]. Despite the reduction in H^+ in the inner magnetosphere, for case A the pseudo Dst is

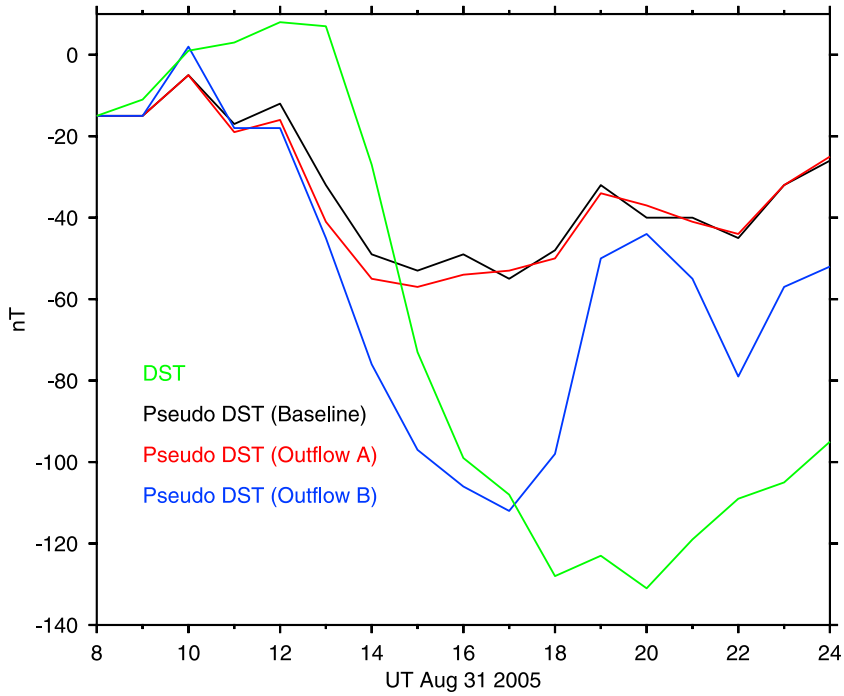

Figure 9. Dst and pseudo Dst for baseline, case A, and case B.

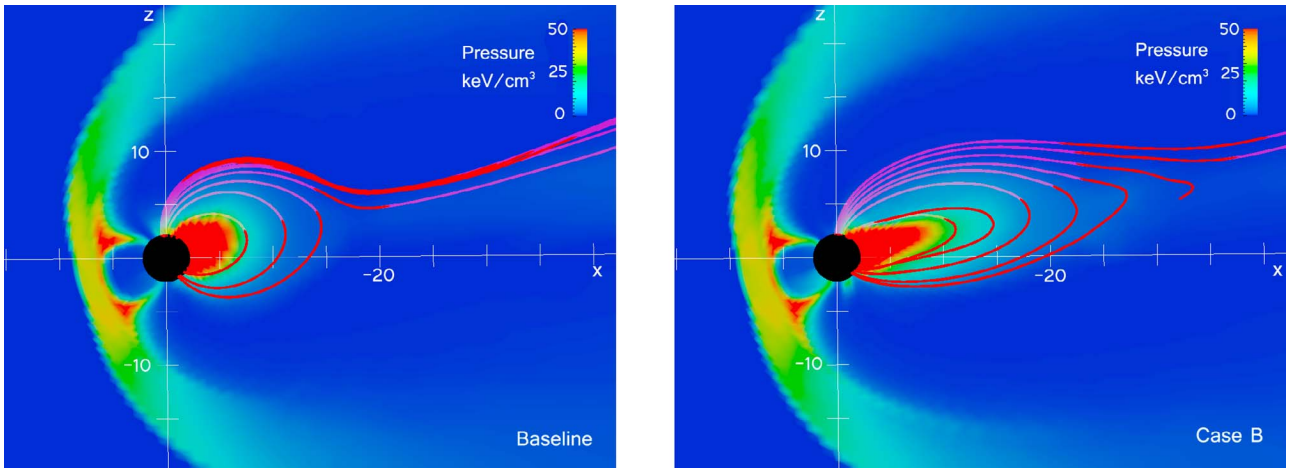

Figure 10. Total plasma pressure for (left) baseline (right) and case B in GSM x-z plane at 1500 UT showing select nightside magnetic field lines.

slightly reduced by up to 10% compared to the baseline simulation, owing to the presence of O^+ ions in the inner magnetosphere. Both the pseudo Dst for baseline and case A simulations compare poorly to the actual Dst.

[30] With outflow case B, the pseudo Dst is reduced to a magnitude comparable to the observed Dst. The magnitude of the pseudo Dst for case B exceeds that of the baseline by a factor of 2, reaching approximately −110 nT, compared to the actual Dst of −137 nT. However, the pseudo Dst still exhibits more variability and recovers earlier than the actual Dst. The pseudo Dst begins to recover at 1700 UT when the southward IMF turns briefly northwards. In contrast, the actual Dst continues to decrease until 2000 UT and decays more slowly.

[31] The pseudo Dst for case B is reduced compared to the baseline simulation because much of the outflowing fluid from the cusp accumulates in the inner magnetosphere. When the outflow is cold and slow, it becomes entrained in the convection cycle and fills the region of nightside closed magnetic field lines (see Figure 7), resulting in a larger radial pressure gradient. The increased pressure gradient generates a larger diamagnetic ring current that reduces the pseudo Dst. The pressure gradient and ring current are approximately twice as large for case B compared to the baseline or case A.

[32] The enhanced ring current in case B also affects the tail dynamics, but differently than in case A. The strong diamagnetic ring current generates a positive B_z tailward of the ring current, producing an enhanced magnetic field normal to the reconnecting current sheet. The local reconnection rate is reduced as a consequence [*Pritchett*, 2005], so the nightside reconnection location moves further downtail where the effect of the ring current and the normal component is lessened (Figure 10). At 1500 UT for the baseline, the nightside reconnection is at approximately 18 R_E, whilst for case B it is at approximately 32 R_E. In case B, $v_{||}/v_{\perp}$ for H^+ in the tail is increased by a factor of approximately 3, meaning that despite the tailward movement of the reconnection line, the access of solar wind ions into the plasmasheet is reduced. When the southward IMF fluctuates northwards at 1700 UT the magnetic field lines reconfigure during a substorm. About 30% of the O^+ density in the inner magnetosphere is lost at the dayside boundary due to the increased convection during the substorm. The flow-out loss causes a reduction in the pressure gradient and an early recovery of the pseudo Dst. After the substorm, the outflow fluence is reduced to about 25% of its values during the main sequence of the magnetic cloud interval (see Figure 4). Consequently, the effect of outflow on the magnetosphere subsides at this time and the nightside field lines return to a configuration comparable to the baseline simulation.

[33] The enhanced pressure gradient in the inner magnetosphere in case B, compared to case A and the baseline substantially reduces the pseudo Dst. However, without a drift kinetic ring current model, the inner magnetosphere in the simulations is controlled by convection rather than gradient curvature drift kinetics, causing the ring current to decay too quickly. Coupling a ring current model, such as the Rice Convection Model to the LFM global simulation may moderate the early recovery of the ring current described here. *Glocer et al.* [2009a] report a similar behaviour in pseudo Dst and a more realistic recovery when a polar wind outflow and the Rice Convection Model are coupled to the BATS-R-US global model. Corotation, not included in this model, may also reduce the decay of the ring current. Plasma on corotating field lines should not be affected by the convective surge from the substorm and therefore less pressure will be lost from the inner magnetosphere. However, corotation is expected to be a small effect compared to the gradient curvature kinetics.

[34] During the main phase of the storm and its recovery, the observed location of nightside reconnection line is predominantly at a distance greater than 30 R_E [*Ohtani and Mukai*, 2008]. This is in general agreement with case B for the main phase of the storm but not during recovery, due to the fast decay of the ring current. The reconnection locations of both case A and the baseline simulation are both more earthward than the analysis by *Ohtani and Mukai* [2008] suggests. In the simulations by *Glocer et al.* [2009a], which coupled both PWOM and RCM to BATS-R-US, the nightside reconnection location is generally beyond 30 R_E.

This suggests that to accurately model the magnetosphere tail dynamics requires ion outflow that is entrained into the inner magnetosphere and a drift kinetic ring current.

4.3. Magnetosphere-Ionosphere Interaction

[35] The ionospheric characteristics for the northern hemisphere for the August 31, 2005 storm are shown in Figure 11. Both outflow case A and B exhibit a decrease in integrated field-aligned current, mean dayside Pedersen conductance and integrated hemispheric and dayside precipitating electron energy flux. For case A, the cross polar cap potential (CPCP) is larger than the baseline whilst it is smaller in case B.

[36] When outflow is included in the simulation the most dramatic change in both cases, A and B, is seen in the electron precipitation power, which is reduced by approximately 50%. In the MFLFM precipitation model implemented here, the electron precipitating number flux depends sensitively on the H^+ number density at the inner boundary. When O^+ outflow is included in the multifluid simulation, the H^+ number density at the nightside inner boundary is decreased due to the reduced access of the solar wind ions into the inner magnetosphere as discussed in the previous section. In the baseline simulation, the H^+ density in the inner magnetosphere reaches approximately 20/cc whilst for case A and B the density is 10/cc and 13/cc respectively. This result is consistent with the results by *Winglee et al.* [2005], who found that high ionospheric outflows aid in the exclusion of light solar wind fluid from the plasmasheet.

[37] The reduction in H^+ plasma density at the inner boundary of the magnetospheric domain results in a lower electron precipitating number flux because the flux of precipitating electrons scales with the H^+ density at the inner boundary. Figure 11 shows that for case A, the average electron energy is relatively unchanged compared to the baseline whilst it is reduced by up to 20% for case B. It is therefore primarily the lower electron precipitating number flux (F_{en}) that causes the decrease in dayside and hemispheric integrated electron precipitating power, which is the integral of $F_{en}\,\overline{E}$ where $\overline{E}$ is the mean electron energy.

[38] The recirculated O^+ fluid at the inner boundary should also influence electron precipitation. However, by not including the effects of O^+ on precipitation in regions of O^+ outflow, we have also effectively neglected its effects in regions of O^+ downflow. (A different and perhaps more realistic strategy would treat the effects of the O^+ population on precipitation differently depending on whether its field-aligned velocity is upward or downward near the inner boundary.) The inclusion of the recirculated O^+ fluid in the inner magnetospheric region where the outflow is zero would increase the electron number and energy fluxes by approximately 20%. This number is estimated from the simulation by calculating the electron precipitating number flux and energy based on the density and pressure of the combined H^+ and O^+ fluids at the inner boundary rather than just H^+ alone as is done in the simulation. The result is an increase in the precipitating electron power from approximately 0.22 TW to 0.27 TW during the main phase of the storm. The estimated power including the effect of O^+ thus remains substantially less than the 0.5 TW of the baseline simulation. Therefore inclusion of recirculated O^+ in the LFM precipitation model is expected to be a minor correction to the results.

[39] Figure 11 also shows the estimated hemispheric power in electron precipitation derived from the NOAA-15,16,17,18 satellites (see http://www.swpc.noaa.gov/ftpdir/lists/hpi/power_2005.txt). For the storm period, the hemispheric power in precipitation in the baseline simulation is a factor of 2–5 larger than the power derived from the NOAA satellites. When outflow is included, the simulated power in precipitation is noticeably reduced, bringing the simulation results in better agreement the NOAA results. This improvement suggests that the exclusion of light solar wind fluid from the inner magnetosphere when O^+ outflow is present is an important physical effect and makes the exclusion of O^+ from the electron precipitation calculation more plausible.

[40] The 50% reduction in dayside electron precipitation is accompanied by a 15% decrease in dayside Pedersen conductance and 10% reduction in integrated field-aligned current in Figure 11. The CPCP for case A increases by approximately 10% compared to the baseline simulation, whilst it decreases up to 20% for case B.

4.4. CPCP and the SW - Magnetosphere Interaction

[41] Nonsteady solar wind conditions during storms and the complicated magnetic geometry of the solar wind-magnetosphere interaction make a quantitative evaluation of the MHD forces acting in the magnetosheath difficult. The following analysis and discussion of this section is therefore more qualitative in nature than in previous sections. It builds on results and insights from other simulation studies.

[42] The less intense Region I currents in both outflow simulations relative to the baseline case indicates that, in the outflow simulations, less current is diverted across the magnetopause into the magnetosheath, where it closes on the bow shock [*Siebert and Siscoe*, 2002; *Siscoe et al.*, 2004; R. E. Lopez et al., The role of magnetosheath force balance in regulating the dayside reconnection potential, submitted to *J. Geophys. Res.*, 2010]. The comparatively weaker $\mathbf{j} \times \mathbf{B}$ force in the magnetosheath is thus less effective in diverting the upstream flow around the subsolar magnetopause in the outflow simulations. Other factors being the same, the magnetic flux delivered to the dayside magnetopause effectively increases, along with the reconnection rate at the magnetopause and/or the effective length of the reconnection line. The implication is a larger dayside reconnection potential and a larger CPCP. This increase in CPCP is observed in case A, but not case B.

[43] In case B, inflation of the magnetosphere by an enhanced ring current counteracts the effect of a weaker $\mathbf{j} \times \mathbf{B}$ force in the magnetosheath. As shown in Figure 12, the shape of the inflated magnetosphere becomes wider and blunter and, consequently, the standoff distance of the bow shock increases [e.g., *Petrinec*, 2002], by as much as 20% in case B relative to the baseline. With an increased standoff distance, the postshock flow has a greater distance to brake and be diverted around the magnetopause by the prevailing $-\nabla p$ and $\mathbf{j} \times \mathbf{B}$ forces. The effect of a wider and blunter magnetosphere has been analyzed by *Merkine et al.* [2003, 2005] when the effective increase in size is due to an increase in the Region I currents, but the same basic effect of magnetospheric inflation on the magnetosheath flow is also

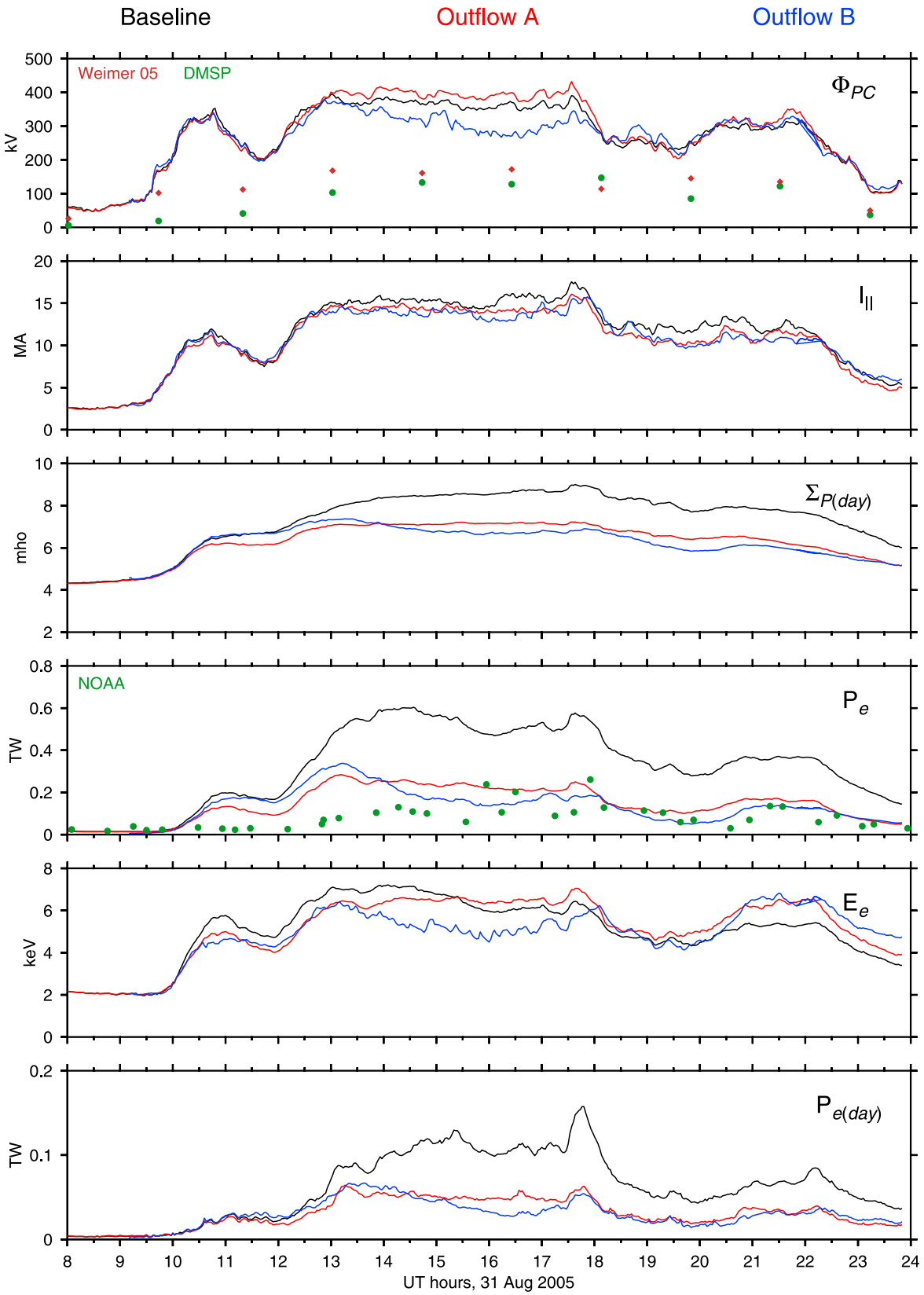

Figure 11. Timeline of ionospheric characteristics from the simulations for the northern hemisphere. (top panel) Cross polar cap potential (with DMSP and Weimer model), (second panel) integrated field-aligned current, (third panel) average dayside Pedersen conductance, (fourth panel) integrated precipitating electron power (with estimate from NOAA satellite data), (fifth panel) average electron energy, (sixth panel) integrated dayside precipitating electron power.

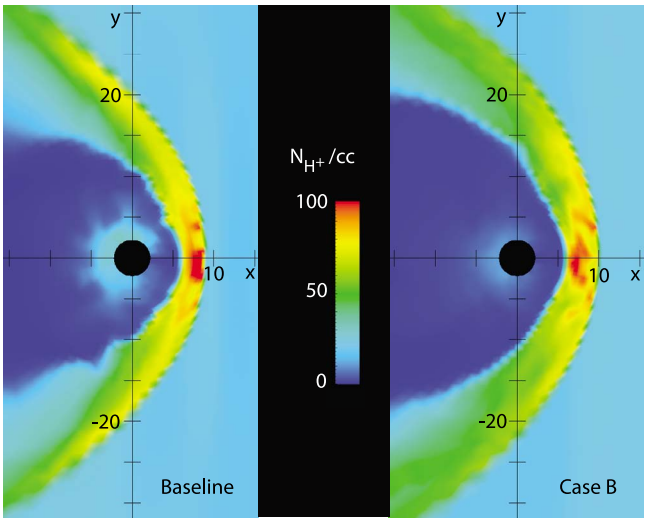

Figure 12. Proton density for (left) baseline and (right) case B in SM x-y plane at 1630 UT.

operative when the increase is due to an enhanced ring current. The enhanced flow diversion now reduces the magnetic flux delivered to the magnetopause, as well as the reconnection potential there and the CPCP. After 1800 UT, when the ring current has decayed, the magnetopause is no longer inflated and the CPCP returns to the baseline. Thus inflation of the magnetosphere by an enhanced ring current induced by cusp O^+ outflow overwhelms the effect of the reduction in Region I current in case B, leading to the simulated decrease in the CPCP.

[44] Figure 11 compares the CPCP from the simulations with the CPCP calculated from the DMSP F-13 satellite (http://cindispace.utdallas.edu/DMSP/) and the Weimer empirical model (http://ccmc.gsfc.nasa.gov/cgi - bin/run_weimer.cgi). SuperDARN did not obtain reliable data during this storm due to the lack of low-latitude radars and because radar backscatter is typically reduced in the summer ionosphere, which is the northern ionosphere for this event [*Ruohoniemi and Greenwald*, 1997]. The CPCP, derived from both DMSP data and the Weimer model are lower than in the simulations. During the magnetic cloud the CPCP is approximately 130 kV from DMSP, 170 kV from the Weimer empirical model, 375 kV for the baseline simulation, 410 kV for case A and 300 kV for case B. The track of the DMSP satellite does not go through the potential minima and maxima and, therefore, its measure of the CPCP is a lower bound on the actual CPCP. (It is noted that large offset potentials were present in DMSP-inferred electric fields at UT 16:26, 18:08 and 19:50. These offsets may render the DMSP-inferred CPCP unreliable at such times.) The inputs to the Weimer empirical model included the solar wind and IMF conditions at 25 R_E on the x-axis, lagged by 18 minutes. This lag is the estimated time for the solar wind to propagate from 25 R_E, through the bowshock to the magnetopause. Since the Weimer model is an empirical average, with more constraining data and, therefore, better statistics for moderate rather than storm time conditions, its estimate of the CPCP is also likely to be lower than the actual CPCP. Nevertheless, the MFLFM simulation most likely overestimates the CPCP. However, as with Dst, the CPCP from outflow case B is significantly improved when compared to data.

[45] These simulations suggest that ion outflow can regulate the solar wind - magnetosphere interaction and the CPCP in two very different ways: 1) by changing the characteristics of electron precipitation, the ionospheric conductance and the Region I current intensity, a portion of which closes in the magnetosheath; and 2) by enhancing the ring current and inflating the magnetosphere. Both effects are manifested by changes in the magnetosheath flow, magnetic flux transport to the magnetopause, and the dayside reconnection potential. For the 31 August 2005 storm, the average energy flux of precipitating electrons is less when cusp outflow is included because the access of the solar wind proton fluid to the inner magnetosphere is diminished by the outflow-induced reconfiguration of the convective pathway of solar wind plasma through the cusp/mantle, lobes and plasmasheet. This particular outcome, namely reduced solar wind proton access to the inner magnetosphere, may not be universal. Storms with different time histories may give rise to different magnetotail configurations. Furthermore, the outflow model in the simulations reported here includes only cusp O^+ outflow. Polar wind H^+ outflow and mixed H^+/O^+ auroral outflows will likely introduce other effects in the precipitation and ionospheric characteristics. Alternatively, the tendency for a reduction in the CPCP due to storm time magnetospheric inflation by an O^+-rich ring current is almost certainly a universal effect.

[46] Both *Winglee et al.* [2002] and *Glocer et al.* [2009a] report a decrease in CPCP when outflow is included, as in case B. This finding is not surprising because, as discussed in Section 4, the O^+ outflow characteristics for case B are similar to the polar wind outflows included in these previous simulations of storms - though not necessarily the local time - latitude distribution of outflow. Case A represents a more realistic specification of cusp O^+ outflow characteristics than case B and, in contrast, leads to a modest increase in the CPCP. This difference suggests that the energy and location of the outflow are important factors in the M-I response to ionospheric outflows and their magnetospheric transport.

[47] In comparing results from the three global simulations models with ionospheric outflows included, it is important to recognize that, in addition to the different treatments of outflow, each model also treats electrodynamic feedback between the magnetosphere and ionosphere differently. The MFLFM model explicitly treats electron precipitation and its nonlinear effects on the ionospheric conductance through the *Robinson et al.* [1987] empirical model for Pedersen and Hall conductances. Proxy variables for the mean energy and flux of the electron precipitation are derived from MHD state variables [*Wiltberger et al.*, 2004]. The BATS-R-US model also uses an empirical conductance model but with dynamic, nonlinear regulation based on the local value of thefield-aligned current rather than precipitation per se [*Ridley et al.*, 2004]. The conductance model used by Winglee includes a three-cell deep resistive layer near the low-altitude simulation boundary [*Winglee*, 1998], wherein a constant scalar resistivity is included in the Ohm's law. Feedback between MHD state variables and the resistivity are not included. As a consequence, the MI

coupling characteristics predicted by these models can be expected to differ in detail.

5. Summary

[48] In this paper, a causally driven cusp O^+ outflow algorithm has been added to the multifluid Lyon-Fedder-Mobarry global simulation, based upon empirical relationships and specifications from *Strangeway et al.* [2005], *Bouhram et al.* [2004], and *Lennartsson et al.* [2004]. Two specifications of outflow were simulated and compared to a baseline run with no outflow for the August 31, 2005 storm. Case A represented a transversely accelerated source with a parallel velocityof 50 km/s and temperature of 100 eV whilst case B represented a colder, slower, more polar wind like source with a parallel velocity of 3 km/s and temperature of 1 eV.

[49] More outflow was released during periods of large B_Z and solar wind ram pressure with a higher fluence in the summer hemisphere. In case A, the effect of the outflow on the M-I dynamics is limited because the majority of the outflow simply flows downtail. A small decrease of 10% in pseudo DST was found, compared to the baseline simulation. The outflow caused a 50% reduction in electron precipitation that resulted in a reduction in ionospheric conductance and integrated field aligned current. It is thought that the reduction in Region I currents leads to less perpendicular currents in the magnetosheath that reduces the $\mathbf{j} \times \mathbf{B}$ force and diverts less flux around the magnetopause. This process results in a higher reconnection potential and a 20% increase in the CPCP.

[50] The outflow in case B was mostly convected into the inner magnetosphere. The enhanced density in the inner magnetosphere doubled the pressure gradient, increasing the diamagnetic ring current and causing a 100% decrease in the pseudo Dst compared to the baseline simulation. However, without a drift kinetic ring current model, the inner magnetosphere is strongly affected by substorm convection that leads to the premature decay of the ring current. The enhanced ring current acts to inflate the magnetosphere, making the magnetopause blunter and increasing the bow shock stand off distance by up to 20%. Increasing the magnetosheath width allows more room for the post shock flow to brake and therefore more flux to be diverted around the magnetosphere, reducing the need for reconnection. Despite a reduction in Region I currents as in case A, the inflation of the magnetosphere is sufficient to cause a 20% decrease in CPCP.

Appendix A: Description of Regulating Functions

[51] In the model, the empirical relationship from *Strangeway et al.* [2005] that drives the O^+ outflow is modified through the use of three additional regulating functions:

$$F_O = 2.14 \times 10^7 S_{\parallel}^{1.265} M_x M_{v_x} M_{F_{en}} \quad \text{(A1)}$$

where M_x and M_{vx} are spatial and convection velocity masks and $M_{F_{en}}$ is a regulator based on the electron number flux (F_{en}) derived from the MFLFM precipitating precipitation model. These masks restrict the outflow to the cusp, the region of interest for this study.

[52] An outflow regulator based on precipitating electron number flux is motivated by 1) its high correlation with O^+ outflow flux in the cusp, as reported by *Strangeway et al.* [2005] and 2) its effects in enhancing the topside plasma density and thus the number of ions available as a source of outflow [*Liu et al.*, 1995]. The $M_{F_{en}}$ mask takes the form

$$M_{F_{en}}(\Lambda, \phi) = \min\left(\frac{F_{en}(\Lambda, \phi)}{F_{en(baseline)}}, 1\right) \quad \text{(A2)}$$

where Λ is invariant latitude and ϕ is the magnetic local time. If the electron number flux exceeds the baseline then $M_{F_{en}}$ is set to 1. The baseline function was tuned so that an equinox simulation for a southward IMF of 5 nT, a solar wind speed of 400 km/s, solar wind density of 5/cc and a sound speed of 40 km/s yielded total O^+ fluences of between $1–2 \times 10^{24}$ ions/s which is the same order of magnitude but generally less than the fluence at 1 R_E altitude reported by *Lennartsson et al.* [2004]. Since the outflow is restricted to the cusp it is expected that fluence rates are below the observed statistical averages. $F_{en(baseline)}$ for this study is set to 1.25×10^8 electrons/cm^2-s. The relative absence of precipitation over the polar cap eliminates the possibility of O^+ outflow over the polar cap, which would otherwise be stimulated by the downward Poynting flux which powers the closure between dawn and dusk Region I currents.

[53] The spatial mask, M_x, limits the outflow to the dayside so that $M_x = 1$ if $x_{SM} > 0$ and $M_x = 0$ if $x_{SM} < 0$. The convection velocity mask, $M_{vx} = 1$ if $v_x < 0$ and $M_{vx} = 0$ if $v_x > 0$ where v_x is the x_{SM} component of the iononospheric convection velocity. This filter eliminates outflows that may arise where downward D.C. Poynting fluxes feed Joule dissipation accompanying the low-latitude closure of Region I and Region II currents with each other.

[54] **Acknowledgments.** The research was supported by the NASA Sun-Earth Connection Theory Program (grant NNX08AI36G), the NASA Living With a Star Targeted Research and Technology Program (grant NNX07AQ16G) and the Center for Integrated Space Weather Modeling funded by the NSF STC program under cooperative agreement ATM-0120950. Computing resources for the research were provided by the National Center for Atmospheric Research under CISL Project 36761008.

[55] Robert Lysak thanks Alex Glocer and another reviewer for their assistance in evaluating this paper.

References

Bouhram, M., B. Klecker, and W. Miyake (2004), On the altitude dependence of transversely heated O+ distributions in the cusp/cleft, *Ann. Geophys.*, *22*, 1787–1798.

Chaston, C. C., C. W. Carlson, J. P. McFadden, R. E. Ergun, and R. J. Strangeway (2007), How important are dispersive Alfvn waves for auroral particle acceleration?, *Geophys. Res. Lett.*, *34*, L07101, doi:10.1029/2006GL029144.

Chun, F., D. J. Knipp, M. G. McHarg, J. R. Lacey, G. Lu, and B. A. Emery (2002), Joule heating patterns as a function of polar cap index, *J. Geophys. Res.*, *107*(A7), 1119, doi:10.1029/2001JA000246.

Damiano, P., W. Lotko, O. Brambles, M. Wiltberger, and J. Lyon (2010), Effects of solar wind IMF and dynamic pressure on the ionospheric O+ fluence during the August 31, 2005 storm, *J. Geophys. Res.*, doi:10.1029/2010JA015583, in press.

Ebihara, Y., M. Yamada, S. Watanabe, and M. Ejiri (2006), Fate of outflowing suprathermal oxygen ions that originate in the polar ionosphere, *J. Geophys. Res.*, *111*, A04219, doi:10.1029/2005JA011403.

Fedder, J. A., S. P. Slinker, J. G. Lyon, and R. D. Elphinstone (1995), Global numerical simulation of the growth phase and the expansion onset for

substorm observed by Viking, *J. Geophys. Res.*, *100*(A10), 19,083–19,093, doi:10.1029/95JA01524.
Gagne, J. (2005), Implementation of ionospheric outflow in the lfm global mhd magnetospheric simulation, M.S. thesis, Dartmouth Coll., Hanover, N. H.
Glocer, A., G. Toth, T. Gombosi, and D. Welling (2009a), Modeling ionospheric outflows and their impact on the magnetosphere, initial results, *J. Geophys. Res.*, *114*, A05216, doi:10.1029/2009JA014053.
Glocer, A., G. Toth, Y. J. Ma, T. Gombosi, J.-C. Zhang, and L. M. Kistler (2009b), Multifluid Block-Adaptive-Tree Solar wind Roe-type Upwind Scheme: Magnetospheric composition and dynamics during geomagnetic storms-Initial results, *J. Geophys. Res.*, *114*, A12203, doi:10.1029/2009JA014418.
Gorney, D., A. Clarke, D. Croley, J. Fennell, J. Luhmann, and P. Mizera (1981), The distribution of ion beams and conics below 8000 km, *J. Geophys. Res.*, *86*(A1), 83–89.
Hultqvist, B., H. Vo, R. Lundin, B. Aparicio, P.-A. Lindqvist, G. Gustafsson, and B. Holback (1991), On the upward acceleration of electrons and ions by low-frequency electric field fluctuations observed by Viking, *J. Geophys. Res.*, *96*(A7), 11609–11615.
Kistler, L. M., C. G. Mouikis, B. Klecker, and I. Dandouras (2010), Cusp as a source for oxygen in the plasma sheet during geomagnetic storms, *J. Geophys. Res.*, *115*, A03209, doi:10.1029/2009JA014838.
Klumpar, D. (1979), Transversely accelerated ions: An ionospheric source of hot magnetospheric ions, *J. Geophys. Res.*, *84*(A8), 4229–4237.
Knudsen, D. J., B. A. Whalen, T. Abe, and A. Yau (1994), Temporal evolution and spatial dispersion of ion conics: Evidence for a polar cusp heatingwall, in *Solar System Plasmas in Space and Time*, *Geophys. Monogr. Ser.*, vol. 84, edited by J. L. Burch and J. H. Waite Jr., 163–169, AGU, Washington, D. C.
Lennartsson, O. W., H. L. Collin, and W. K. Peterson (2004), Solar wind control of Earth's H + and O + outflow rates in the 15-eV to 33-keV energy range, *J. Geophys. Res.*, *109*, A12212, doi:10.1029/2004JA010690.
Liu, C., J. L. Horwitz, and P. G. Richards (1995), Effects of frictional ion heating and soft-electron precipitation on high-latitude F-region upflows, *Geophys. Res. Lett.*, *22*(20), 2713–2716.
Lockwood, M., J. H. Waite Jr., T. E. Moore, J. F. E. Johnson, and C. R. Chappell (1985a), A new source of suprathermal O+ ions near the dayside polar cap boundary, *J. Geophys. Res.*, *90*, 4099–4116.
Lockwood, M., M. O. Chandler, J. L. Horwitz, J. H. Waite Jr., T. E. Moore, J. F. E. Johnson, and C. R. Chappell (1985b), The cleft ion fountain, *J. Geophys. Res.*, *90*, 9736–9748.
Lyon, J., J. Fedder, and C. Mobarry (2004), The Lyon-Fedder-Mobarry (LFM) global MHD magnetospheric simulation code, *J. Atmos. Sol. Terr. Phys.*, *66*, 1333–1350, doi:10.1016/j.jastp.2004.03.020.
Merkine, V. G., K. Papadopoulos, G. Milikh, A. S. Sharma, X. Shao, J. Lyon, and C. Goodrich (2003), Effects of the solar wind electric field and ionospheric conductance on the cross polar cap potential: Results of global MHD modeling, *Geophys. Res. Lett.*, *53*(9), 2180, doi:10.1029/2003GL017903.
Merkine, V. G., A. S. Sharma, K. Papadopoulos, G. Milikh, J. Lyon, and C. Goodrich (2005), Relationship between the ionospheric conductance, field aligned current, and magnetopause geometry: Global MHD simulations, *Planet. Space Sci.*, *30*, 873–879, doi:10.1016/j.pss.2005.04.001.
Newell, P. T., T. Sotirelis, K. Liou, C.-I. Meng, and F. J. Rich (2006), Cusp latitude and the optimal solar wind coupling function, *J. Geophys. Res.*, *111*, A09207, doi:10.1029/2006JA011731.
Norqvist, P., M. Andr, and M. Tyrland (1998), A statistical study of ion energization mechanisms in the auroral region, *J. Geophys. Res.*, *103*(A10), 23,459–23,473.
Ohtani, S., and T. Mukai (2008), Statistical characteristics of the storm time plasma sheet, *J. Geophys. Res.*, *113*, A01221, doi:10.1029/2007JA012547.
Peterson, W. K., H. L. Collinb, M. Boehm, A. W. Yau, C. Cully, and G. Lu (2002), Investigation into the spatial and temporal coherence of ionospheric out)ow on January 9–12, 1997, *J. Atmos. Sol. Terr. Phys.*, *64*, 1659–1666.
Ridley, A. J., T. I. Gombosi, and D. L. DeZeeuw (2004), Ionospheric control of the magnetosphere: Conductance, *Ann. Geophys.*, *22*, 567–584.
Ridley, A. J., Y. Deng, and G. Tth (2006), The global ionosphere thermosphere model, *J. Atmos. Sol. Terr. Phys.*, *68*, 839–864.
Petrinec, S. M. (2002), The location of the Earth's bow shock, *Planet. Space Sci.*, *50*, 541–547.
Pilipp, W. G., and G. Morfill (1978), The formation of the plasmasheet resulting from plasma mantle dynamics, *J. Geophys. Res.*, *83*, 5670–5678.
Pritchett, P. L. (2005), The "Newton Challenge": Kinetic aspects of forced magnetic reconnection, *J. Geophys. Res.*, *110*, A10213, doi:10.1029/2005JA011228.
Robinson, R. M., R. R. Vondrak, K. Miller, T. Babbs, and D. A. Hardy (1987), On calculating ionospheric conductivities from the flux and energy of precipitating electrons, *J. Geophys. Res.*, *92*, 2565–2569.
Ruohoniemi, J., and R. Greenwald (1997), Rates of scattering occurrence in routine HF radar observations during solar cycle maximum, *Radio Sci.*, *32*(3) 1051–1070.
Shelley, E., R. Johnson, and R. Sharp (1972), Satellite observations of energetic heavy ions during a geomagnetic storm, *J. Geophys. Res.*, *77*(31), 6104–6110.
Shelley, E., R. Johnson, and R. Sharp (1976), Satellite observations of an ionospheric Acceleration mechanism, *Geophys. Res.Lett.*, *3*(11), 654–656.
Siebert, K. D., and G. L. Siscoe (2002), Dynamo circuits for magnetopause reconnection, *J. Geophys. Res.*, *107*(A7), 1095, doi:10.1029/2001JA000237.
Siscoe, G. L., G. M. Erickson, B. U. O. Sonnerup, N. C. Maynard, K. D. Siebert, D. R. Weimer, and W. W. White (2001), Relation between cusp and mantle in MHD simulation, *J. Geophys. Res.*, *106*(A6), 10,743–10,749.
Siscoe, G., J. Raeder, and A. J. Ridley (2004), Transpolar potential saturation models compared, *J. Geophys. Res.*, *109*, A09203, doi:10.1029/2003JA010318.
Strangeway, R. J., R. E. Ergun, Y.-J. Su, C. W. Carlson, and R. C. Elphic (2005), Factors controlling ionospheric outflows as observed at intermediate altitudes, *J. Geophys. Res.*, *110*, A03221, doi:10.1029/2004JA010829.
Su, Y.-J., J. Horwitz, T. Moore, B. Giles, M. Chandler, P. Craven, M. Hirahara, and C. Pollock (1998), Polar wind survey with the Thermal Ion Dynamics Experiment Plasma Source Instrument suite aboard POLAR, *J. Geophys. Res.*, *103*(A12), 29,305–29,337.
Suguira, M. (1973), Quiet time magnetospheric field depression at 2.33.6 RE, *J. Geophys. Res.*, *78*(16), 3182–3185.
Thelin, B., B. Aparicio, and R. Lundin (1990), Observations of upflowing ionospheric ions in the midaltitude cusp/cleft region with the Viking satellite, *J. Geophys. Res.*, *95*(A5), 5931–5939.
Whalen, B., W. Bernstein, and P. Daly (1978), Low altitude acceleration of ionospheric ions, *Geophys. Res. Lett.*, *5*(1), 55–58.
Wiltberger, M., W. Wang, A. G. Burns, S. C. Solomon, J. G. Lyon, and C. C. Goodrich (2004), Initial results from the coupled magnetosphere ionosphere thermosphere model: Magnetospheric and ionospheric responses, *J. Atmos. Sol. Terr. Phys.*, *66*(15–16), 1411–1423, doi:10.1016/j.jastp.2004.03.026.
Wiltberger, M., R. S. Weigel, W. Lotko, and J. A. Fedder (2009), Modeling seasonal variations of auroral particle precipitation in a global-scale magnetosphere-ionosphere simulation, *J. Geophys. Res.*, *114*, A01204, doi:10.1029/2008JA013108.
Winglee, R. M. (1998), Multifluid simulations of the magnetosphere: The identification of the geopause and its variation with IMF, *Geophys. Res. Lett.*, *25*, 4441–4444, doi:10.1029/1998GL900217.
Winglee, R. M., D. Chua, M. Brittnacher, G. K. Parks, and G. Lu (2002), Global impact of ionospheric outflows on the dynamics of the magnetosphere and cross-polar cap potential, *J. Geophys. Res.*, *107*(A9), 1237, doi:10.1029/2001JA000214.
Winglee, R. M., W. Lewis, and G. Lu (2005), Mapping of the heavy ion outflows as seen by IMAGE and multifluid global modeling for the 17 April 2002 storm, *J. Geophys. Res.*, *110*, A12S24, doi:10.1029/2004JA010909.
Yau, A. W., and M. André (1997), Sources of ion outflow in the high latitude ionosphere, *Space. Sci. Rev.*, *80*(1–5), 1–25.
Yau, A., E. Shelley, W. Peterson, and L. Lenchyshyn (1985), Energetic auroral and polar ion outflow at DE 1 altitudes: Magnitude, composition, magnetic activity dependence, and long-term variations, *J. Geophys. Res.*, *90*(A9), 8417–8432.
Yee, K. S. (1966), Numerical solution of initial boundary value problems involving Maxwell's equations in isotropic media, *IEEE. Trans. Antennas Propag.*, *14*, 302–307.
Zheng, Y., T. E. Moore, F. S. Mozer, C. T. Russell, and R. J. Strangeway (2005), Polar study of ionospheric ion outflow versus energy input, *J. Geophys. Res.*, *110*, A07210, doi:10.1029/2004JA010995.

O. J. Brambles, P. A. Damiano, W. Lotko, and B. Zhang, Thayer School of Engineering, Dartmouth College, Hanover, NH 03755, USA. (ojbrambles@dartmouth.edu)
J. Lyon, Department of Physics and Astronomy, Dartmouth College, Hanover, NH 03755, USA.
M. Wiltberger, High Altitude Observatory, National Center for Atmospheric Research, 3450 Mitchell Ln., Boulder, CO 80301, USA.